Progress in Photovoltaics:
Research and Applications

Comparison of the ablation and spectroscopic characteristics of thin $CuIn_{1-x}Ga_xSe_2$ solar cell films fabricated by co-evaporation and co-sputtering processes

Journal:	*Progress in Photovoltaics: Research and Applications*
Manuscript ID:	Draft
Wiley - Manuscript type:	Research Article
Date Submitted by the Author:	n/a
Complete List of Authors:	Lee, Seok; GIST, Kim, C. K.; GIST, Shim, H. S.; GIST, RISE Yoo, J. H.; Applied Spectra Inc., Russo, R. E.; LBNL, ; Applied Spectra Inc., Jeong, Sungho; Gwangju Institute of Science and Technology, School of Mechatronics
Keywords:	Solar cell, CIGS, Laser ablation, LIBS

Comparison of the ablation and spectroscopic characteristics of thin $CuIn_{1-x}Ga_xSe_2$ solar cell films fabricated by co-evaporation and co-sputtering processes

S. H. Lee[1], C. K. Kim[1], H. S. Shim[2], J. H. Yoo[3], R. E. Russo[3,4] and S. H. Jeong[1,*]

[1] School of Mechatronics, Gwangju Institute of Science and Technology, 1 Oryong-dong Buk-gu, Gwangju 500-712, Republic of Korea

[2] Research Institute for Solar and Sustainable Energies, Gwangju Institute of Science and Technology, 1 Oryong-dong Buk-gu, Gwangju 500-712, Republic of Korea

[3] Applied Spectra Inc., 46661 Fremont Boulevard, Fremont, California 94538, USA

[4] Lawrence Berkeley National Laboratory, 1 Cyclotron Road, Berkeley, California 94720, USA

ABSTRACT

The influence of fabrication processes on the LIBS (Laser Induced Breakdown Spectroscopy) spectra of major and minor chemical constituents in $CuIn_{1-x}Ga_xSe_2$ (CIGS) absorber films produced by co-sputtering and co-evaporation techniques on Mo-coated soda lime glass (SLG) is reported. It was found that the ablation rate per pulse of CIGS layers fabricated by the co-sputtering technique is higher than those fabricated by the co-evaporation technique, resulting in higher LIBS signal intensities of the constituent elements. The examination of surface morphology of irradiated surfaces and changes in LIBS signal intensities revealed evidences of elemental fractionation for the CIGS films fabricated by co-sputtering technique but not for those by co-evaporation technique. From x-ray diffraction measurements, it was confirmed that the differences in the ablation and spectroscopic characteristics of the two different types of CIGS

absorber films were contributed to the differences in crystalline properties. Furthermore, it was demonstrated that LIBS can effectively determine a depth profile of sodium concentration in CIGS thin films, diffused from SLG.

KEYWORDS

Solar cell, CIGS, Ablation, LIBS

***Correspondence**

Sungho Jeong, School of Mechatronics, Gwangju Institute of Science and Technology, Gwangju 500-712, Republic of Korea.

E-mail: shjeong@gist.ac.kr

1. INTRODUCTION

The second generation solar cells based on thin absorber layers such as amorphous silicon (*a-Si*), CdTe, or $CuIn_{1-x}Ga_xSe_2$ (CIGS) have several advantages as compared to the first generation solar cells based on crystalline silicon (*c-Si*). For example, thin film solar cells can be manufactured at a lower cost than the *c-Si* counterparts [1]. Also, due to manufacturability on flexible substrates, thin film solar cells can be easily integrated into the roof or exterior walls of a building [2]. Accordingly, there have been tremendous research efforts to enhance the photo-conversion efficiency of thin film solar cells and to develop cost-effective manufacturing technologies. Among the various types of thin film solar cells, CIGS solar cells offer several attractive properties for practical solar power applications such as high absorption coefficient and high photo-conversion efficiency of greater than 20% [3, 4]. The high absorption coefficient of CIGS absorbing layer allows the effective film thickness to be in the range of only 1 ~ 2 microns, greatly reducing the material usage and associated costs compared to *c-Si* solar cells.

The fabrication of thin CIGS absorbing layer can be achieved by various methods that include sputtering [5-8], co-evaporation [9-11], electrodeposition [12], spray pyrolysis [13], paste coating [14] etc. Among these techniques, co-evaporation (shortly, evaporation) and co-sputtering (shortly, sputtering) processes are the preferred methods for commercial manufacturing due to process scalability to mass production with consistent and high photo-conversion efficiency performance. In the evaporation process, the constituent elements (Cu, In, Ga, and Se) are simultaneously vaporized in a chamber and homogeneous CIGS thin film is then formed by surface reaction on a substrate. The highest cell efficiency of 20.3 % has been recorded from the thin absorber film obtained by three-stage evaporation method [3]. In a two-step sputtering process, the Cu-In-Ga precursor thin films are deposited on the substrate from the

metal targets of Cu, In, Ga or their alloys such as CuGa, CuIn, and In_2Se_3, and the CIGS films are obtained by subsequent reaction with selenium source in the elevated temperature environment. The sputtering-based processes could be more adaptable for large area and continuous fabrication due to its simpler fabrication steps and the availability of existing manufacturing facilities.

Although many factors are known to influence on the efficiency of CIGS solar cell devices, the primary factor that requires most rigorous control is the elemental composition of the CIGS absorber layer. The stoichiometric ratio of main chemical constituents of the CIGS absorber is known to govern its energetic and electronic properties [15-18]. Therefore, an accurate measurement of the elemental composition of CIGS absorber layer is a crucial and challenging issue for the fabrication process development and manufacturing of high efficiency CIGS solar cells. Several analytical methods such as secondary ion mass spectrometry (SIMS) [19], inductively coupled plasma optical emission spectroscopy (ICP-OES) [20], glow discharge mass spectrometry (GDMS) [21], laser induced breakdown spectroscopy (LIBS) [22-23], or x-ray fluorescence (XRF) [3] have been applied for the elemental analysis of solar cells. Among these methods, however, only LIBS and XRF measurements can be performed under atmospheric environment without the need for complex vacuum systems, thereby allowing in-situ monitoring and thus quality control compositional measurements during CIGS films manufacturing. More commonly accepted technique such as ICP-OES requires extensive sample preparation involving acid dissolution of bulk samples and the measurement takes too long for it to be an effective in-line method for production control.

LIBS is a powerful method for elemental analysis in which real-time analysis, high sensitivity, and no sample preparation [24-32] are desired. LIBS has been successfully applied

for environmental monitoring [33-35], biological species detection [36], military applications [37], precious artworks analysis [38], nuclear power station inspection [39], depth profiling of thin film materials [40,41], etc. Recently, Darwiche et al. [22] reported the multi-elemental analytical characterization of different qualities of solid silicon using LIBS, in particular, the investigation of optimal environmental parameters such as the pressure and the composition of buffering gas to improve detection limit of impurities such as boron, calcium and chromium etc. and addressed the application of LIBS for solar cell industry. Since LIBS only requires nano to micro grams of mass for effective analysis, a thin film of 100 nm in thickness or less can be analyzed by LIBS for elemental composition [41]. Consequently, LIBS could be the most effective technique for high-resolution elemental mapping and depth profiling analyses of thin CIGS layers. Furthermore, sodium (Na), one of the key elements governing the efficiency of CIGS solar cells, can be measured with high detection sensitivity down to ppm level using LIBS. This provides LIBS a distinct advantage over XRF due to the XRF technique's ineffectiveness for lighter elements including Na. The short analysis time of LIBS, one second or less per single laser shot measurement [42], is another strong advantage for enabling rapid compositional characterization and implementing real-time quality control in manufacturing lines. Despite these clear advantages of LIBS, the applications of LIBS for elemental analysis of thin film solar cell materials has been hardly investigated and very limited number of research papers [43] have been published for LIBS analysis of CIGS absorber layer up to date.

In this work, we report the results for LIBS analyses of CIGS thin absorber films fabricated by sputtering- and evaporation-based processes. The differences in ablation characteristics and LIBS signal intensity of the CIGS layers fabricated by these two different deposition methods were compared. In addition, their microstructural properties were

investigated by x-ray diffraction (XRD) and scanning electron microscopy (SEM). It is shown that the observed differences between the sputtered and evaporated films are associated with microstructural properties of the CIGS films.

2. EXPERIMENTAL SETUP

The polycrystalline CIGS absorber films were grown by either a three-stage evaporation process or a two-step sputtering process as illustrated in Fig. 1. For substrate, soda-lime glass (SLG) (Abrisa Co.) coated with a Mo layer of below 1 μm thickness was utilized. The Mo layer functions as the back electrode of a solar cell. For the fabrication of evaporated films, In, Ga and Se sources were first simultaneously evaporated at the substrate temperature of 400 °C to form a $(In,Ga)_2Se_3$ layer with a thickness of 1 μm, then as the second step Cu and Se were evaporated and reacted with the $(In,Ga)_2Se_3$ layer at the substrate temperature of 600 °C to form a Cu-rich phase, and finally In, Ga and Se elements were again evaporated maintaining the same substrate temperature to produce a Cu-poor phase. For the sputtered films, a Cu-In-Ga precursor film was first fabricated with the thickness of ca. 0.8 μm by simultaneous sputtering of $Cu_{0.6}Ga_{0.4}$ and $Cu_{0.5}In_{0.5}$ targets, and then the CIGS film was obtained by subsequent selenization reaction between precursor film and the Se source provided from a downstream Se cracker (JMON, Korea) at the substrate temperature of 550 ^{o}C for 80 min.

The differences in crystallographic characteristics of the CIGS thin films prepared by both methods were investigated by XRD measurements (Rigaku X-ray diffractormeter with Cu Kα radiation). The chemical composition and thickness of both CIGS thin films were measured by XRF using the CIGS calibration sample consisting of 18.4 at% Cu, 14.3 at% In, 5.0 at% Ga and 62.3 at% Se with the thickness of 2.15 μm (F12H28F11-2, Calmetrics Inc.) as the reference,

and the results are summarized in Table 1. The CIGS films appeared to have the same thickness but different compositions. The evaporated film was found to be a Cu-poor film ($CuIn_{1.1}Ga_{0.19}Se_{2.32}$), whereas the sputtered film resulted in a Se-poor phase ($CuIn_{0.75}Ga_{0.25}Se_{1.53}$).

LIBS analyses of the two CIGS absorber films were carried out by using a commercial LIBS system (Applied Spectra Inc., Model: RT100-HP). The measurement system was equipped with a high performance Czerny-Turner spectrometer that had a dual-grating turret providing maximum spectral resolution of 0.1 nm with a 40 nm spectral window. A Q-switched Nd:YAG laser (λ=1064 nm, τ=4ns) with a near top-hat spatial profile was used to generate plasma with a fixed spot diameter of 150 μm.

For LIBS measurement, ten laser pulses were successively shot on the same spot of each sample at the rate of 1 Hz and the evolution of LIBS spectra with respect to pulse number was examined. SEM (Hitach S-4700) images of the ablated surfaces at different pulse numbers were taken to check the changes in surface morphology.

3. RESULTS AND DISCUSSION

Fig. 2 shows the typical LIBS spectra of the two types of CIGS sample over the spectral ranges of 298-338 and 395-418 nm, separated by a break line. The laser energy used for these measurements was 0.48 mJ, corresponding to laser fluence of 2.72 J/cm^2, and the gate delay was 0.5 μs. These values of laser pulse energy and gate delay yielded the maximum signal to background ratio (SBR) and minimum full width at half maximum (FWHM) of the LIBS emission lines of analyzed chemical constituents. In general, the emission peak intensities of the constituent elements reflect the original concentration of those elements within the target, although the relation between the ratio of actual concentration and the ratio of LIBS signal

intensities needs to be further examined for precise calibration. Thus, the intensity ratios of Ga/(Ga+In) for both sputtered and evaporated CIGS films were calculated with Ga(I) peak at 403.299 nm and In(I) peak at 410.176nm in Fig. 2 and compared. The calculated Ga/(Ga+In) intensity ratios of the sputtered and evaporated films were 0.33 and 0.28, respectively, implying that Ga concentration in the sputtered film is higher than that in the evaporated film. Similar trends were obtained when other Ga and In peaks in Fig. 2 were used for the same calculation. The relatively higher Ga concentration of the sputtered film than that of the evaporated film predicted by these LIBS spectra agrees with the XRF measurement results shown in Table 1.

While it is understood that the intensity ratios between elements revealed consistency with the original composition, the intensities of emission lines for the sputtered CIGS film appears significantly higher than those of the evaporated CIGS film over the entire spectral range in Fig. 2. The higher emission lines' intensities of the sputtered film can be observed more clearly for early gate delays as shown in Fig. 3 where the intensity differences of the In(I) emission line at 410.176 nm between the sputtered and evaporated films are shown. Note, however, that the In concentration measured by XRF in Table 1 showed a slightly lower value for the sputtered film. Since an enhanced peak intensity in LIBS spectra is a direct result of increased electron population in laser plasma [44], the observed relatively higher peak intensities of the sputtered film is considered to imply that a higher electron population was attained within the sputtered-film laser plasma. It is assumed that since both films were made of the same constituting elements, there exist no fundamental differences in the emission transition characteristics of those elements in both films.

From the measured LIBS spectra, the electron number density of laser plasmas produced from the sputtered and evaporated films can be estimated as follows. First, it was assumed that

the FWHM of the measured intensity peaks was determined mainly by the Stark effect and instrumental characteristics. Then, the electron density could be found from the following relation [45],

$$\frac{\Delta\lambda_{Stark}}{n_e} \approx \left(\frac{2w_{ref}}{n_e^{ref}}\right) \quad (3)$$

where $\Delta\lambda_{Stark}$ is the Stark broadened FWHM, n_e is the electron density, and w_{ref} is the reference width for a reference electron density n_e^{ref}. Since the observed line width ($\Delta\lambda_{observed}$) is contributed from both Stark effect and instrumental resolution ($\Delta\lambda_{instrumental}$), $\Delta\lambda_{Stark}$ was obtained by [46],

$$\Delta\lambda_{Stark} = \Delta\lambda_{observed} - \Delta\lambda_{instrumental} \quad (4)$$

The electron density n_e was then calculated by Eq. (3) using the measured line width of Cu emission line at 324.754 nm and the known reference values of w_{ref} = 0.0095 nm and n_e^{ref} = 0.66 × 10^{17} cm^{-3} for Cu [47]. To obtain $\Delta\lambda_{Stark,\,Cu}$ in Eq. (4), $\Delta\lambda_{observed}$ was extracted from the Lorentz fitting of the measured Cu peak (Fig. 4) and $\Delta\lambda_{instrumental}$ was replaced by the resolution of the ICCD camera used in experiments (0.1 nm). The electron number densities calculated by using Eqs. (3) and (4) are shown in Fig. 5 as a function of gate delays. As shown in Fig. 5, the electron density of the sputtered film was calculated to be higher than that of the evaporated film for all gate delays, which reconfirms the observed higher intensity in Fig. 2.

The higher spectral intensity in Fig. 2 and the higher computed electron number density in Fig. 5 of the sputtered film are considered to confirm that a stronger atomization and ionization has taken place on the sputtered film. Since laser ablation conditions were identical for both films, the observed higher emission line intensities of CIGS elements for the sputtered film were related to an enhanced ablation rate. To verify ablation rate difference between the sputtered and

evaporated films, spectral changes of these films with respect to laser pulse number were examined. Specifically, the LIBS spectra of both samples were recorded as shown in Figs. 6(a) and 6(b), and the detection of Mo emission lines at 386.411 and 390.296 nm was used to determine the point at which the laser ablation of Mo layer starts to occur. Note that the thicknesses of the two types of CIGS layers were the same at 1.23 μm. The variation of In, Ga and Mo intensities, normalized by the maximum value obtained over the ten pulses, is summarized as a function of laser pulse number as shown in Fig. 7. In the case of sputtered film (Fig. 7 (a)), the intensity of Mo peak increased sharply at the 4^{th} pulse, indicating that it took four laser pulses to remove the entire CIGS layer. Conversely, the intensities of Ga and In peaks dropped rapidly after the 4^{th} shot. For the evaporated film, the increase of Mo peak intensity and the drop of In and Ga intensities were observed at the 8^{th} pulse (Fig. 7 (b)). The examination of the ablated surfaces of these two types of CIGS films revealed completely different ablation and crater morphological characteristics as shown in Fig. 8. Note that the surfaces of both samples had similar structures prior to laser irradiation. First, the low magnification (x250) images of the ablation craters in Figs. 8(a) and 8(b) show that the CIGS films were ablated nearly uniformly over the entire laser spot for both samples until some uneven crater bottom profile emerge at increased pulse numbers. After the first pulse, however, the surface of sputtered film starts to develop a porous appearance (Fig. 8(a)), possibly due to fractional ablation of the different constituent elements. With increasing pulse number, the porous look of the surface becomes less apparent because of the melting and subsequent re-solidification of the ablated surface. At the 4^{th} shot, the CIGS layer was ruptured in the middle revealing the underlying layer (Mo), which marked the sharp increase of Mo signal intensity at the 4^{th} pulse in Fig. 7(a). Note that the Ga line intensity of the sputtered film in Fig. 7(a) increased until the 4^{th} laser pulse, whereas that of

In peak showed a continuous decrease, which can be an indication of preferential vaporization of the different constituent elements. If LIBS analysis is performed with an assumption that peak intensity is proportional to the original composition of the sample, the elemental fractionation, possibly observed for the sputtered film could become the source of measurement errors for the elemental composition of CIGS layers. On the other hand, the evaporated film showed a completely different surface morphology after the 1st shot, that is, a uniform melting of the surface with no porosity (Fig. 8(b)). The surface morphology of the evaporated film remained almost the same for increasing pulse numbers until a rupture took place in the middle at the seventh shot which also marked the sudden increase of Mo signal intensity in Fig. 7(b). The observed consistency in the morphology of the ablated surface for the evaporated film by the laser pulse number 2 through 6 may be an indication of mass removal with reduced elemental fractionation, and have led to more consistent intensity ratio of Ga and In peaks in Fig. 7(b). These results imply that more accurate estimation of elemental concentration could be achieved by just considering LIBS intensity measurements alone for the evaporated film.

It is known that the fractional ablation can occur due to different alloy structure of composites even for the same element [48]. The observed differences in LIBS spectra and ablation morphologies between the sputtered and evaporated films were understood to be closely related to micro-structural differences of the CIGS layers fabricated by the two methods. For the verification of structural differences, XRD measurements were carried out and the results are shown in Fig. 9(a). The peaks related to a CIGS crystal are observed at 17.9, 27.6, 36.5, 45.2, 53.4, 63.7, 65.4, and 72.2^{o}, which represent (101), (112), (211), (220), (312), (323), (400) and (332) crystal planes for a chalcopyrite structures, respectively (JCPDS 86-1503) [49]. The XRD patterns revealed the existence of tetragonal chalcopyrite crystal structure for both samples,

which was confirmed by the main peaks appeared at (112), (220), (312), (400) and (332) planes of the chalcopyrite structure [50, 51]. However, the (101) and (323) peaks are absent in the sputtered film data. In general, relatively stronger peak intensities were observed for the evaporated film over the characteristic peaks, implying higher crystalline properties of the evaporated film than the sputtered film. The crystalline characteristics of the sputtered and evaporated films were also examined with cross-sectional SEM images as shown in Fig. 9(b), which clearly show that large crystal grains were produced in the evaporated film, whereas the sputtered film yielded small, rounded, granular microstructure with poorly defined grain size. The observed large number of grain boundaries in the sputtered film is considered to have contributed to a relatively stronger absorption of the incident laser energy. Note that impurity is another factor that is closely related to laser energy absorption but little impurity signals were observed in the LIBS data of both films. These results from XRD and SEM measurements demonstrate that the crystalline properties of the CIGS absorber layers vary with fabrication processes, which in turn results in the differences in spectroscopic characteristics during LIBS elemental analysis of these layers.

Finally, it is shown that Na profile along the depth of CIGS layers due to diffusion from the SLG substrate during fabrication process can be determined by LIBS. Na content in the CIGS layer is one of the crucial factors governing solar cell efficiency [53]. For the measurement of Na content, the intensity variation of Na line at 589.593nm was examined with varying laser pulse numbers as shown in Fig. 10. Based on the data in Fig. 7, the laser pulses up to the 4^{th} shot and 8^{th} shot for the sputtered and evaporated films, respectively, were considered for the Na profile examination. For both samples, it is observed that the Na concentration near the surface and near the CIGS-Mo interface was higher than that in the bulk area, which agrees with the previous

study that reported a high Na content in the surface regime and a nearly uniform distribution in the bulk [52, 53]. These results demonstrate the potential for in-situ depth profiling of CIGS layers with LIBS.

4. CONCLUSION

In this work, LIBS elemental analysis of the absorber layer of CIGS solar cells fabricated by two different methods, co-sputtering and co-evaporation processes, was carried out in order to investigate how the fabrication process influences on the LIBS spectra. It was found that the LIBS intensity of the constituent elements of the sputtered film is significantly higher than that of the evaporated film of similar composition and the same thickness. On the contrary, the sputtered film revealed evidences of possible preferential vaporization of different elements that must be accounted for accurate estimation of elemental composition by LIBS. On the other hand, the evaporated film showed a high consistency in the individual line intensities. The observed differences in LIBS signal characteristics between the CIGS films fabricated by two different types of technique were found to originate from the fundamental differences in crystalline properties of the CIGS layers produced by the two methods. These results confirm that the critical parameters for LIBS elemental analysis of CIGS solar cells should include the fabrication process and resulting material characteristics.

ACKNOWLEDGMENT

This work was supported by the National Research Foundation of Korea (NRF) grant funded by the Korea government (MEST) (No. 2011-0029850).

REFERENCES

[1] Chopra KL, Paulson PD, Dutta V. Thin-film solar cells: an overview. *Progress in Photovoltaics: Research and Applications* 2004; **12**: 69-92.

[2] Pagliaro M, Ciriminna R, Palmisano G. Flexible solar cells. *ChemSusChem* 2008; **1**: 880-891.

[3] Jackson P, Hariskos D, Lotter E, Paetel S, Wuerz R, Menner R, Wischmann W, Powalla M. New world record efficiency for Cu(In,Ga)Se_2 thin-film solar cells beyond 20%. *Progress in Photovoltaics: Research and Applications* 2011; **19**: 894-897.

[4] Green MA, Emery K, Hishikawa Y, Warta W. Solar cell efficiency tables (version 37). *Progress in Photovoltaics: Research and Applications* 2011; **19**: 84-92.

[5] Marudachalam M, Birkmire RW, Hichri H, Schultz JM, Swartzlander A, Al-Jassim MM. Phases, morphology, and diffusion in $CuIn_xGa_{1-x}Se_2$ thin films. *Journal Applied Physics* 1997; **82**: 2896–2905.

[6] Kushiya K, Ohshita M, Hara I, Tanaka Y, Sang B, Nagoya Y, Tachiyuki M, Yamase O. Yield issues on the fabrication of 30 cm × 30 cm-sized Cu(In,Ga)Se_2-based thin-film modules. *Solar Energy Materials and Solar Cells* 2003; **75**: 171–178.

[7] Nishiwaki S, Satoh T, Hashimoto Y, Negami T, Wada T. Preparation of Cu(In,Ga)Se_2 thin films at low substrate temperatures. *Journal of Materials Research* 2001; **16**: 394-399.

[8] Dimmler B, Dittrich H, Schock HW. Structure and morphology of evaporated bilayer and selenized $CuInSe_2$ films. *Proceedings of the 20th IEEE Photovoltaic Solar Energy*

Conference, Las Vegas, 1988; 1426–1430.

[9] Tuttle JR, Contreras M, Tennant A, Albin D, Noufi R. High efficiency thin-film Cu(In,Ga)Se_2-based photovoltaic devices: progress towards a universal approach to absorber formation. *Proceedings of the 23rd IEEE Photovoltaic Specialists Conference*, New York, 1993; 415–421.

[10] Gabor AM, Tuttle JR, Albin DS, Contreras MA, Noufi R, Hermann AM. High-efficiency $CuIn_xGa_{1-x}Se_2$ solar cells made from $(In_x,Ga_{1-x})_2Se_3$ precursor films. *Applied Physics Letters* 1994; **65**: 198-200.

[11] Zweigart S, Walter Th, Koble Ch, Sun SM, Ruhle U, Schock HW. Sequential deposition of Cu(In,Ga)$(S,Se)_2$," *Proceedings of the lst IEEE World Conference on Photovoltaic Energy Conversion*, Hawaii, 1994; 60–67.

[12] Hodes G, Lokhande CD, Cahen D. The flexibility of electrodeposition for preparation of $CuInS(Se)_2$ films. *Journal of Electrochemistry Society* 1986; **133**: C113.

[13] Krunks M, Kijatkina O, Rebane H, Oja I, Mikli V, Mere A. Composition of $CuInS_2$ thin films prepared by spray pyrolysis. *Thin Solid Films* 2002; **403-404**: 71–75.

[14] Kaelin M, Rudmann D, Kurdesau F, Zogg H, Meyer T, Tiwari AN. Low-cost CIGS solar cells by paste coating and selenization. *Thin Solid Films* 2005; **480-481**: 486-490.

[15] Mudryi AV, Gremenok VF, Karotki AV, Zalesski VB, Yakushev MV, Luckert F, Martin R. Structural and optical properties of thin films of Cu(In,Ga)Se_2 semiconductor compounds. *Journal of Applied Spectroscopy* 2010; **77**: 371-377.

[16] Wei SH, Zhang SB, Zunger A. Effects of Ga addition to $CuInSe_2$ on its electronic, structural, and defect properties. *Applied Physics Letters* 1998; **72**: 3199-3201.

[17] Dullweber T, Hanna G, Shams-Kolahi W, Schwartzlander A, Contreras MA, Noufi F, Schock HW. Study of the effect of gallium grading in $Cu(In,Ga)Se_2$. *Thin Solid Films* 2000; **361-362**: 478-481.

[18] Ishizuka S, Yamada A, Matsubara K, Fons P, Sakurai K, Niki S. Alkali incorporation control in $Cu(In,Ga)Se_2$ thin films using silicate thin layers and applications in enhancing flexible solar cell efficiency. *Applied Physics Letters* 2008; **93**: 124105.

[19] Durose K, Asher SE, Jaegermann W, Levi D, McCandless BE, Metzger W, Moutinho H, Paulson PD, Perkins CL. Sites JR, Teeter G, Terheggen M. Physical Characterization of Thin-film Solar Cells. *Progress in Photovoltaics: Research and Applications* 2004; **12**: 177-217.

[20] Martinuzzi S, Perichaud I, Trassy C, Degoulange J. n-Type Multicrystalline Silicon Wafers Prepared from Plasma Torch Refined Upgraded Metallurgical Feedstock. *Progress in Photovoltaics: Research and Applications* 2009; **17**: 297-305.

[21] Modanese C, Sabatino MD, Søiland AK, Peter K, Arnberg L. Investigation of bulk and solar cell properties of ingots cast from compensated solar grade silicon. *Progress in Photovoltaics: Research and Applications* 2011; **19**: 45-53.

[22] Darwiche S, Benmansour M, Eliezer N, Morvan D. Laser-induced breakdown spectroscopy for photovoltaic silicon wafer analysis. *Progress in Photovoltaics: Research and Applications* 2011; DOI: 10. 1002/pip. 1209.

[23] Hidalgo M, Martin F, Laserna JJ. Laser-induced breakdown spectrometry of titanium Dioxide Antireflection Coatings in Photovoltaic Cells. *Analytical Chemistry* 1996; **68**: 1095-1100.

[24] Radziemski LJ. From laser to LIBS, the path of technology development. *Spectrochimica Acta Part B* 2002; **57**: 1109–1113.

[25] Sneddon J, Lee YI. Novel and recent applications of elemental determination by laser-induced breakdown spectrometry. *Analytical Letters* 1999; **32**: 2143-2162.

[26] Song K, Lee YI, Sneddon J. Recent developments in instrumentation for laser induced breakdown spectroscopy. *Applied Spectroscopy Reviews* 2002; **37**: 89-117.

[27] Cremers DA, Radzimski LJ. *Handbook of Laser-Induced Breakdown Spectroscopy*. John Wiley & Sons: England, 2006; 302.

[28] Miziolek A, Palleschi V, Schechter I. *Laser-Induced Breakdown Spectroscopy (LIBS): Fundamentals and Applications*. Cambridge University Press., United Kingdom, Cambridge, 2006; 638.

[29] Russo R, Mao X, Liu H, Gonzalez J, Mao S. Laser ablation in analytical chemistry-a review. *Talanta* 2002; **57**: 425-451.

[30] Tognoni E, Palleschi V, Corsi M, Cristoforetti G. Quantitative micro-analysis by laser-induced breakdown spectroscopy: a review of the experimental approaches. *Spectrochimica Acta Part B* 2002; **57**: 1115–1130.

[31] Fichet P, Menut D, Brennetot R, Vors E, Rivoallan A. Analysis by laser-induced breakdown spectroscopy of complex solids, liquids, and powders with an echelle spectrometer. *Applied Optics* 2003; **42**: 6029–6035.

[32] Vadillo J, Laserna J. Laser-induced plasma spectrometry: truly a surface analytical tool. *Spectrochimica Acta Part B* 2004; **59**: 147–161.

[33] Dudragne L, Adam Ph, Amouroux J. Time-resolved laser-induced breakdown spectroscopy: application for qualitative and quantitative detection of fluorine, chlorine, sulfur, and carbon in air. *Applied Spectroscopy* 1998; **52**: 1321–1327.

[34] Zhang H, Yueh F, Singh J. Laser-induced breakdown spectrometry as a multimetal continuous-emission monitor. *Applied Optics* 1999; **38**: 1459–1466.

[35] Hahn D. Laser-induced breakdown spectroscopy for sizing and elemental analysis of discrete aerosol particles. *Applied Physics Letters* 1998; **72**: 2960–2962.

[36] Samek O, Beddows D, Telle H, Kaiser J, Liska M, Caseres J, Gonzales Urena A. Quantitative laser-induced breakdown spectroscopy analysis of calcified tissue samples. *Spectrochimica Acta Part B* 2001; **56**: 865–875.

[37] Goode SR, Dockery CR, Bachmeyer MF, Nieuwland AA, Morgan SL. Detecting gunshot residue by laser induced breakdown spectroscopy. *OSA Trends in Optics and Photonics*

Series 2002; **81**, 175-177.

[38] Anglos D, Couris S, Fotakis C. Laser Diagnostics of Painted Artworks: Laser-Induced Breakdown Spectroscopy in Pigment Identification. *Applied Spectroscopy* 1997; **51**: 1025–1030.

[39] Whitehouse AI, Young J, Botheroyd IM, Lawson S, Evans CP, Wright J. Remote material analysis of nuclear power station steam generator tubes by laser-induced breakdown spectroscopy. *Spectrochimica Acta Part B* 2001; **56**: 821–830.

[40] Margetic V, Bolshov M, Stokhaus A, Niemax K, Hergenroder R. Depth profiling of multi-layer samples using femtosecond laser ablation. *Journal of Analytical Atomic Spectrometry* 2001; **16**: 616–621.

[41] Owens T, Mao S, Canfield E, Grigoropoulos C, Mao X, Russo R. Ultrafast thin-film laser-induced breakdown spectroscopy of doped oxides. *Applied Optics* 2010; **49**: C67-C69.

[42] Bol'shakov AA, Yoo JH, Liu C, Plumer JR, Russo RE. Laser-induced breakdown spectroscopy in industrial and security applications. *Applied Optics* 2010; **49**: C132-C142.

[43] Lee SH, Shim HS, Kim CK, Yoo JH, Russo RE, Jeong SH. Analysis of the absorption layer of CIGS solar cell by laser-induced breakdown spectroscopy. *Applied Optics* 2012; **51**: B115-B120.

[44] Aguilera J, Aragón C. Characterization of a laser-induced plasma by spatially resolved spectroscopy of neutral atom and ion emissions: Comparison of local and spatially integrated measurements. *Spectrochimica Acta Part B* 2004; **59**: 1861-1876.

[45] Detalle V, Héon R, Sabsabi M, St-Onge L. An evaluation of a commercial Échelle spectrometer with intensified charge-coupled device detector for materials analysis by laser-induced plasma spectroscopy. *Spectochimica Acta Part B* 2001; **56**: 1011-1025.

[46] Sabsabi M, Cielo P. Quantitative Analysis of Aluminum Alloys by Laser-Induced Breakdown Spectroscopy and Plasma Characterization. *Applied Spectroscopy* 1995; **49**: 499-507.

[47] Konjević N, Lesage A, Fuhr JR, Wiese WL. Experimental Stark Widths and Shifts for Spectral Lines of Neutral and Ionized Atoms (A Critical Review of Selected Data for the Period 1989 Through 2000). *Journal of Physical and Chemical Reference Data* 2002; **31**: 819-927.

[48] Fernandez A, Mao XL, Chan WT, Shannon MA, Russo RE. Correlation of Spectral Emission Intensity in the Inductively Coupled Plasma and Laser-Induced Plasma during Laser Ablation of Solid Samples. *Analytical Chemistry* 1995; **67**: 2444-2450.

[49] Kodigala SR. *Thin Films and Nanostructures: Cu($In_{1-x}Ga_x$)Se_2 Based Thin Film Solar Cells*. Elsevier, Amsterdam, Netherlands, 2010; 146-166.

[50] Vidhya B, Velumani S, Arenas-Alatorre J, Morales-Acevedoa A, Asomozaa R, Chavez-Carvayar J. Structrual studies of mechano-chemically synthesized $CuIn_{1-x}Ga_xSe_2$ nano particles. *Materials Science and Engineering: B* 2010; **174**: 216–221.

[51] Suryanarayana C, Yoo S, Groza J. Consolidation of mechanically alloyed Cu-In-Ga-Se powders. *Journal of Materials Science Letters* 2001; **20**: 2179–2181.

[52] Caballero R, Kaufmann C, Eisenbarth T, Cancela M, Hesse R, Unold T, Eicke A, Klenk R, Schock H. The influence of Na on low temperature growth of CIGS thin film solar cells on polymide substrate. *Thin Solid Films* 2009; **517**: 2187-2190.

[53] Mount G, Buyuklimanli T, Michel R, Moskito J, Robie S, Sharma U, Wang L. Investigation of differences between high and low efficiency CIGS solar cell structures using surface analytical techniques. *Proceedings of the 35th IEEE Photovoltaic Special Conference*, Hawaii, 2010; 003466-003471.

Table 1. Composition and thickness of the CIGS absorber films fabricated by co-evaporation and co-sputtering processes measured by XRF

Fabrication method	Thickness (μm)		Composition (%)				Elemental ratio
	CIGS	Mo	Cu	In	Ga	Se	[Ga]/[Ga+In]
Sputtering	1.23	0.57	28.19	21.36	7.28	43.17	0.25
Evaporation	1.23	0.76	21.63	23.83	4.15	50.39	0.15

FIGURE CAPTIONS

Fig. 1. Illustrations for the fabrication of CIGS absorber layer by (a) co-evaporation process and (b) co-sputtering process

Fig. 2. Typical LIBS spectra of the CIGS absorber films fabricated by co-evaporation and co-sputtering processes (gate delay = 0.5μs).

Fig.3. Intensity variations of the In(I) emission line at 410.176 nm of the two types of CIGS film with respect to gate delay.

Fig.4. Fitting of the measured Cu and In emission lines to Lorentz profile for the calculation of electron number density (Data from the evaporated film. Gate delay = 0.5 μs)

Fig.5. Computed electron number density of the two types of CIGS film with respect to gate delay

Fig. 6. LIBS spectra of the Mo lines at 386.411 nm and 390.296 nm of the (a) sputtered and (b) evaporated films

Fig. 7. Variation of the normalized intensities of In, Ga and Mo peaks of the (a) sputtered and (b) evaporated films with respect to laser pulse number.

Fig. 8. SEM images of the ablated surfaces of the (a) sputtered and (b) evaporated films at different laser pulse numbers.

Fig. 9. (a) X-ray diffraction patterns and (b) cross sectional SEM images of the sputtered and evaporated films

Fig. 10. Intensity variation of the Na line at 589.593 nm with respect to laser pulse number.

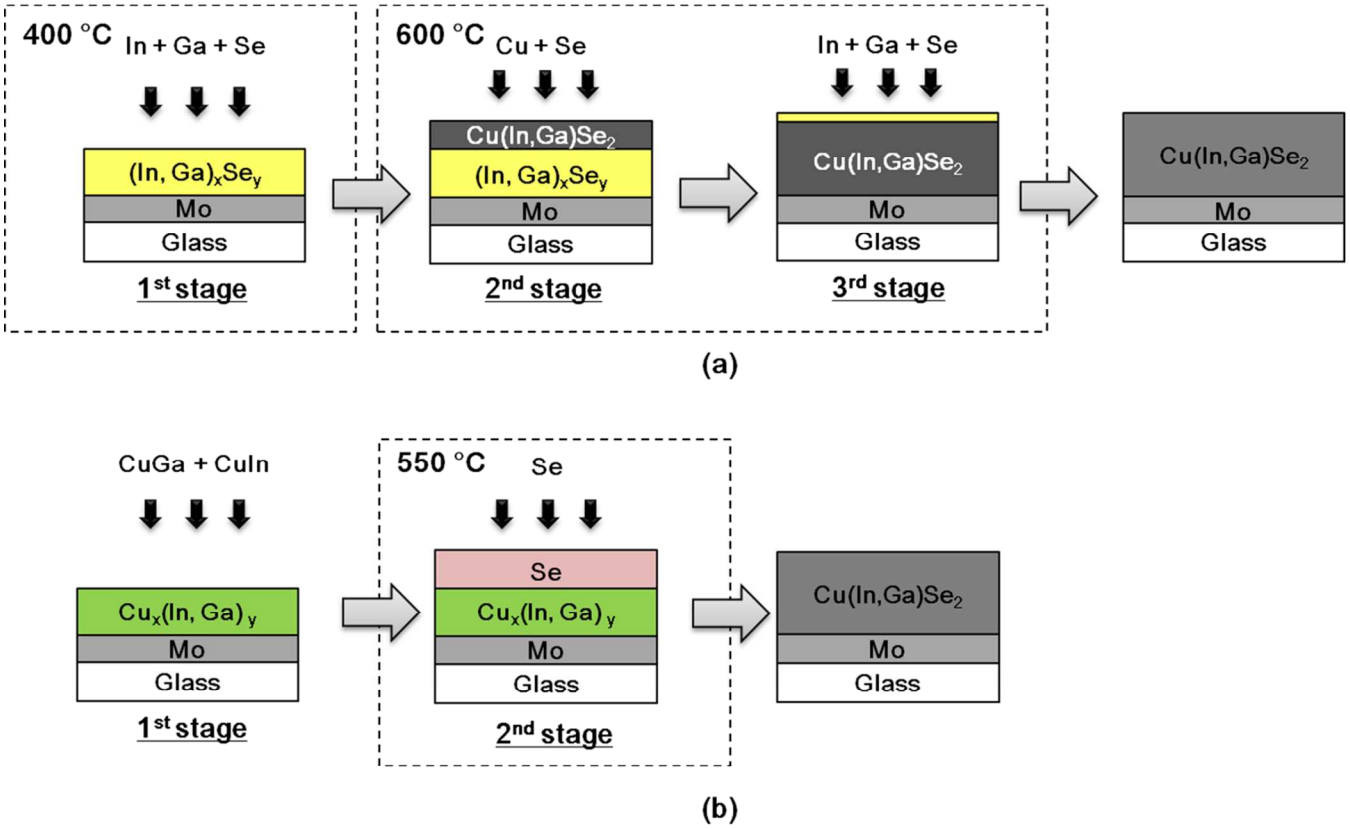

Fig. 1. Illustrations for the fabrication of CIGS absorber layer by (a) co-evaporation process and (b) co-sputtering process

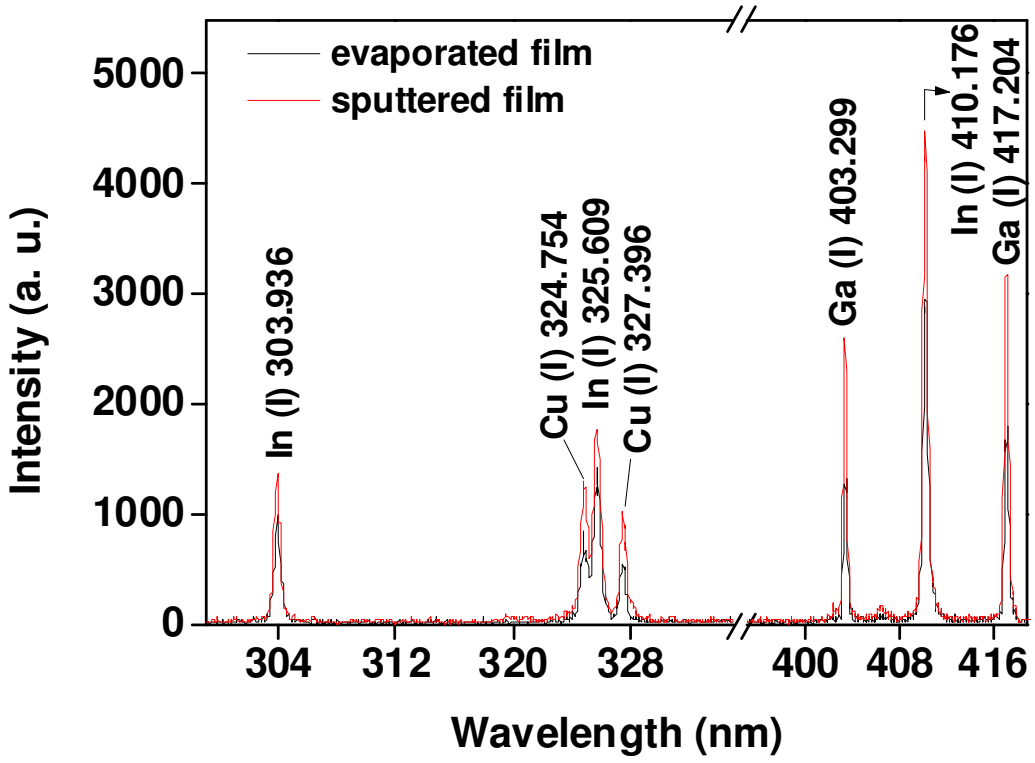

Fig. 2. Typical LIBS spectra of the CIGS absorber films fabricated by co-evaporation and co-sputtering processes (gate delay = 0.5μs).

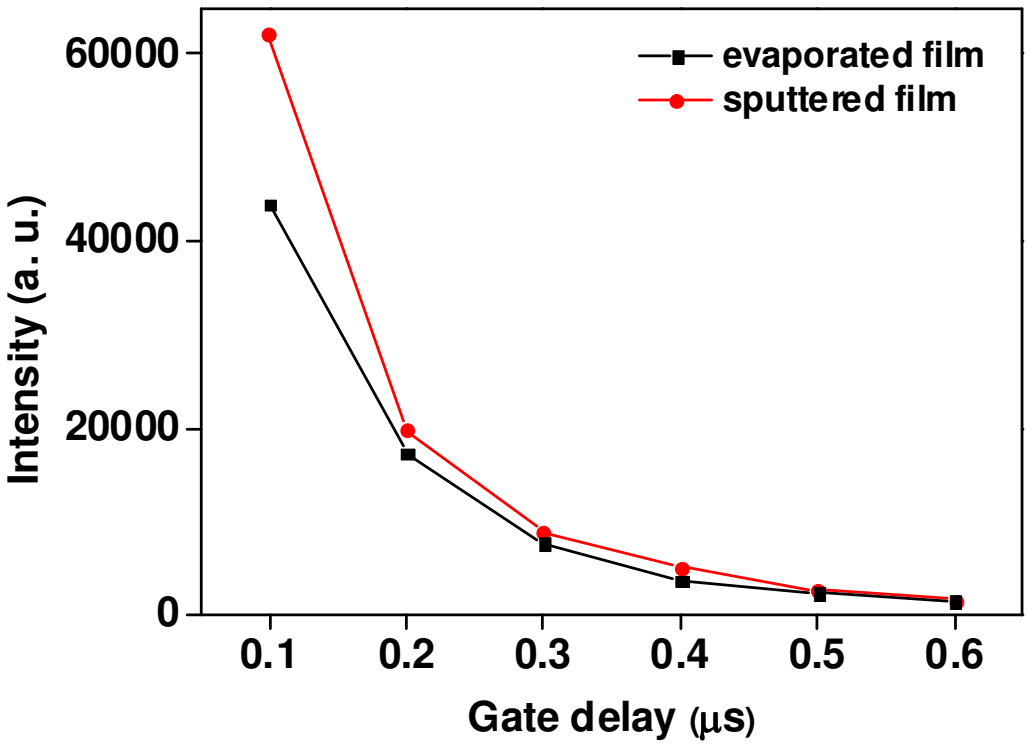

Fig.3. Intensity variations of the In(I) emission line at 410.176 nm of the two types of CIGS film with respect to gate delay.

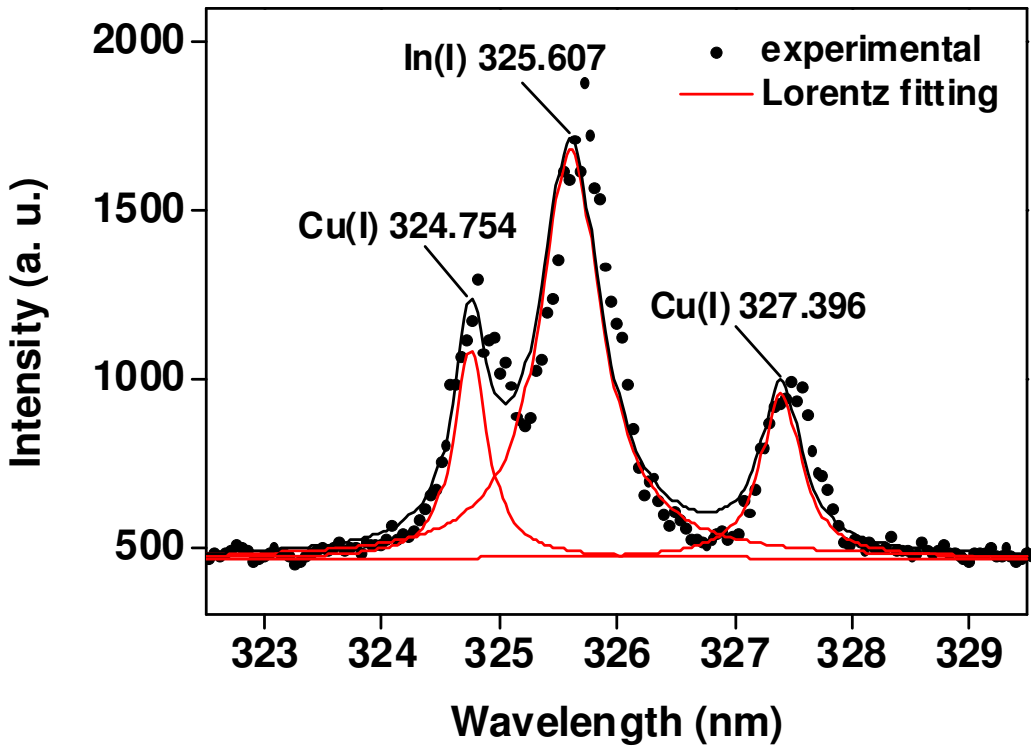

Fig.4. Fitting of the measured Cu and In emission lines to Lorentz profile for the calculation of electron number density (Data from the evaporated film. Gate delay = 0.5 μs)

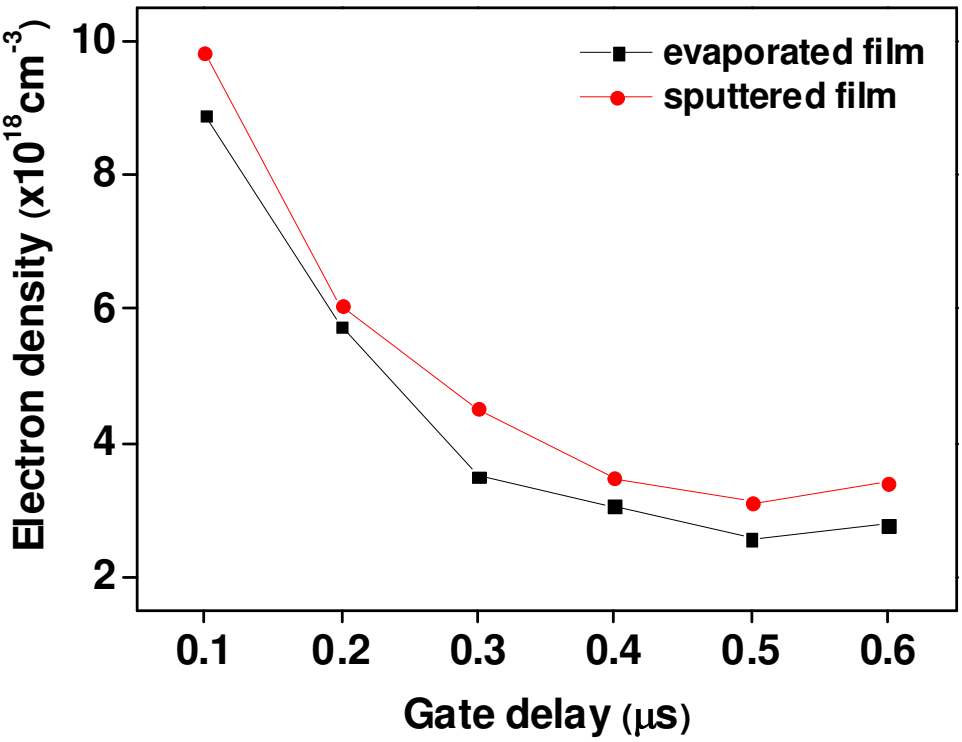

Fig.5. Computed electron number density of the two types of CIGS film with respect to gate delay.

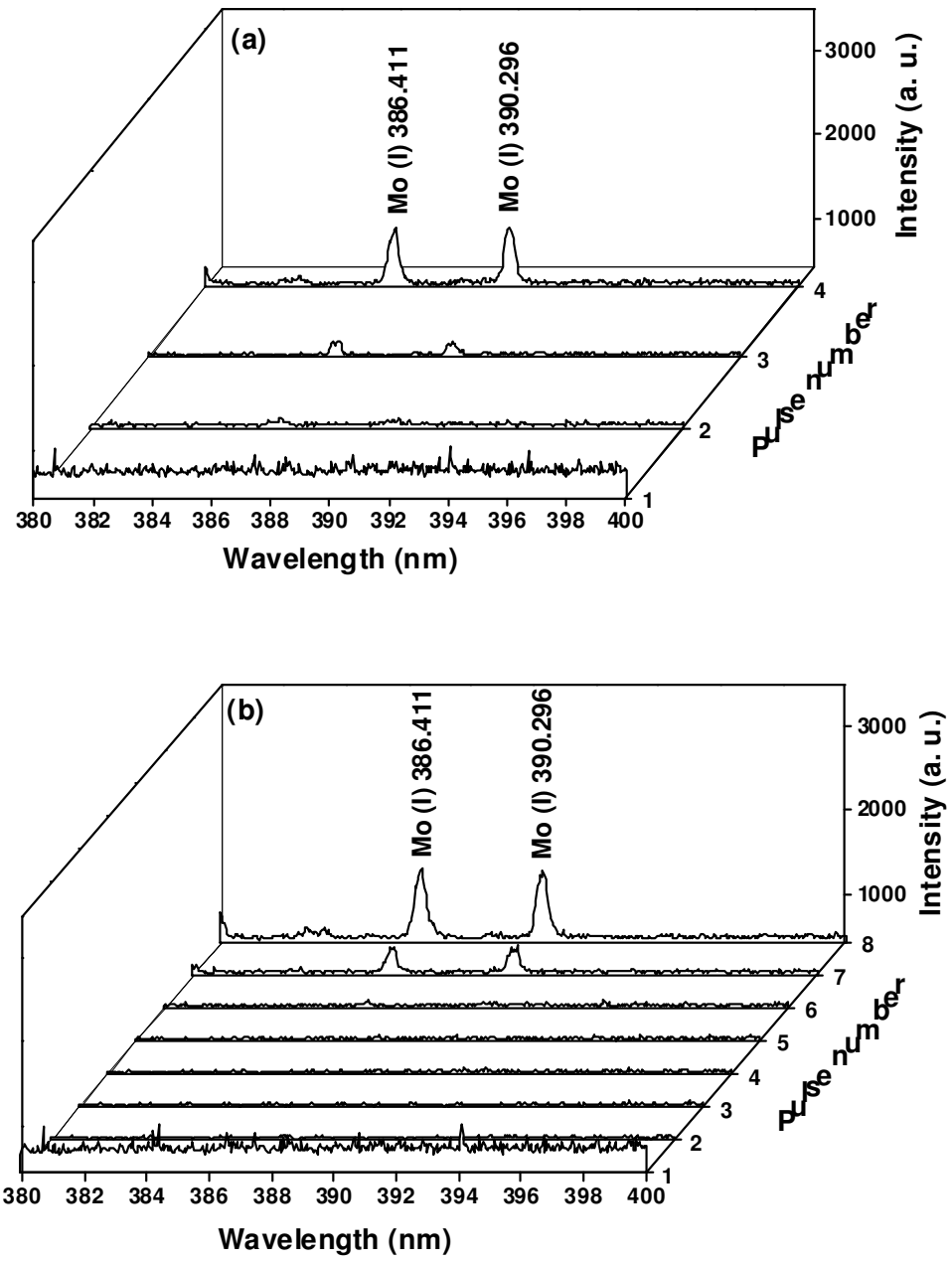

Fig. 6. LIBS spectra of the Mo lines at 386.411 nm and 390.296 nm of the (a) sputtered and (b) evaporated films

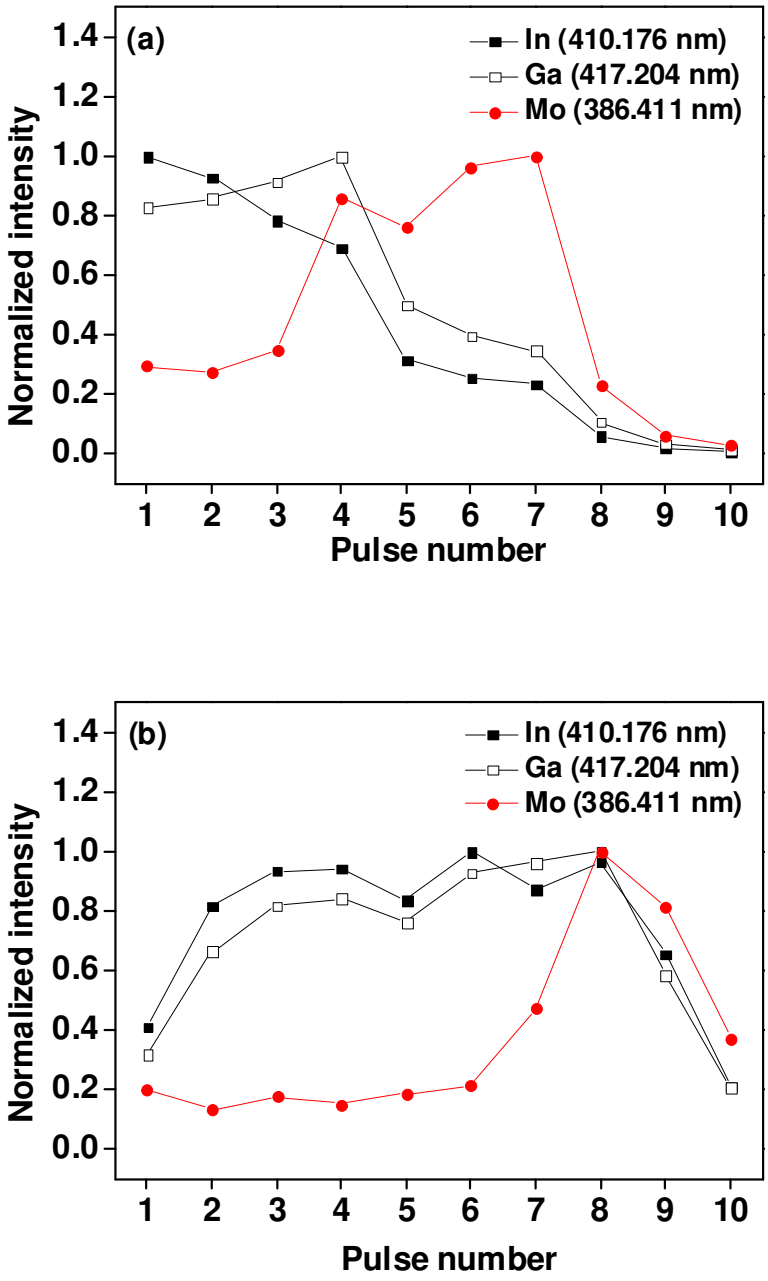

Fig. 7. Variation of the normalized intensities of In, Ga and Mo peaks of the (a) sputtered and (b) evaporated films with respect to laser pulse number.

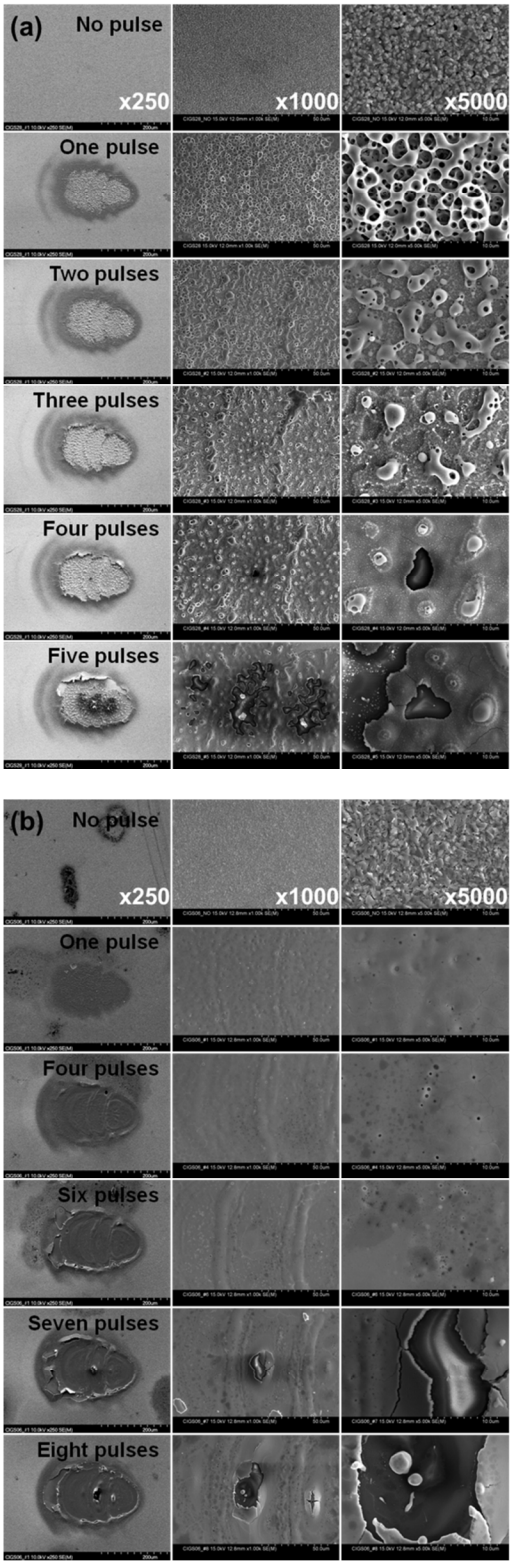

Fig. 8. SEM images of the ablated surfaces of the (a) sputtered and (b) evaporated films at different laser pulse numbers.

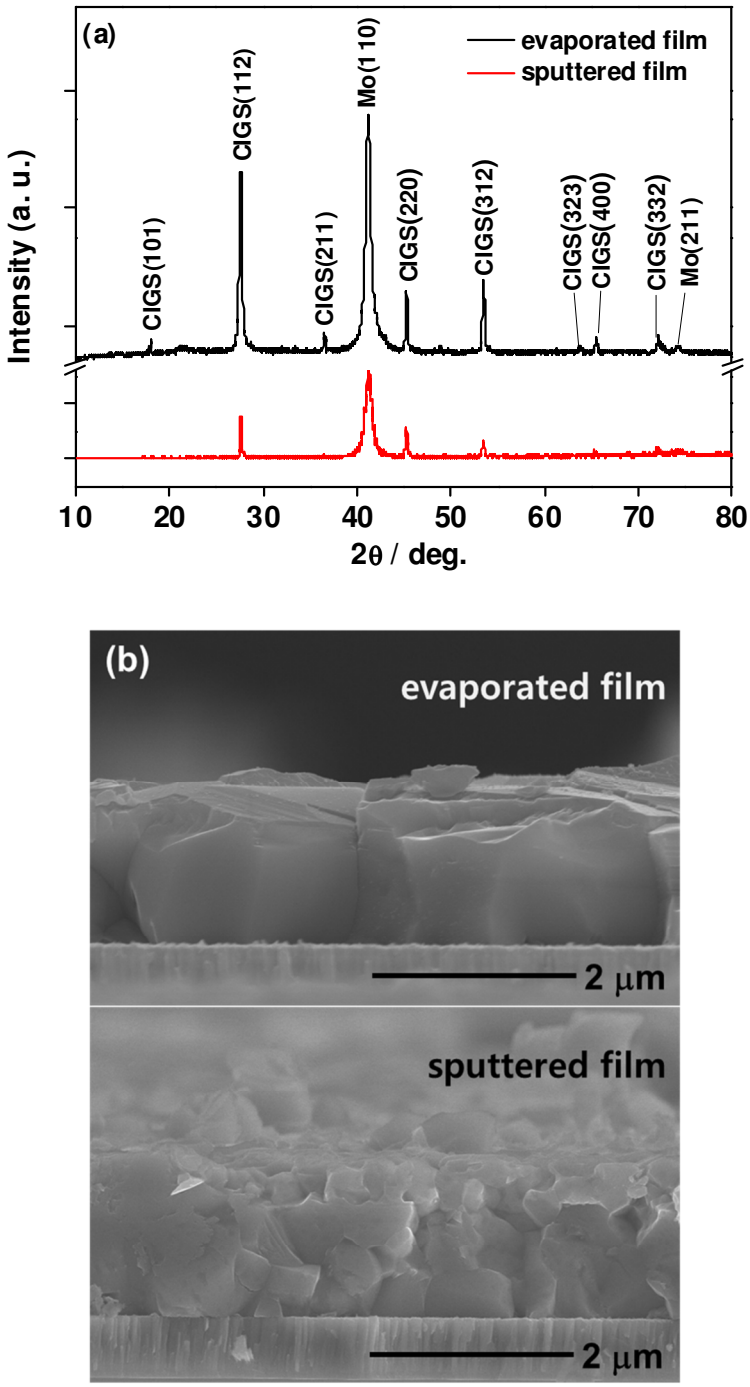

Fig. 9. (a) X-ray diffraction patterns and (b) cross sectional SEM images of the sputtered and evaporated films

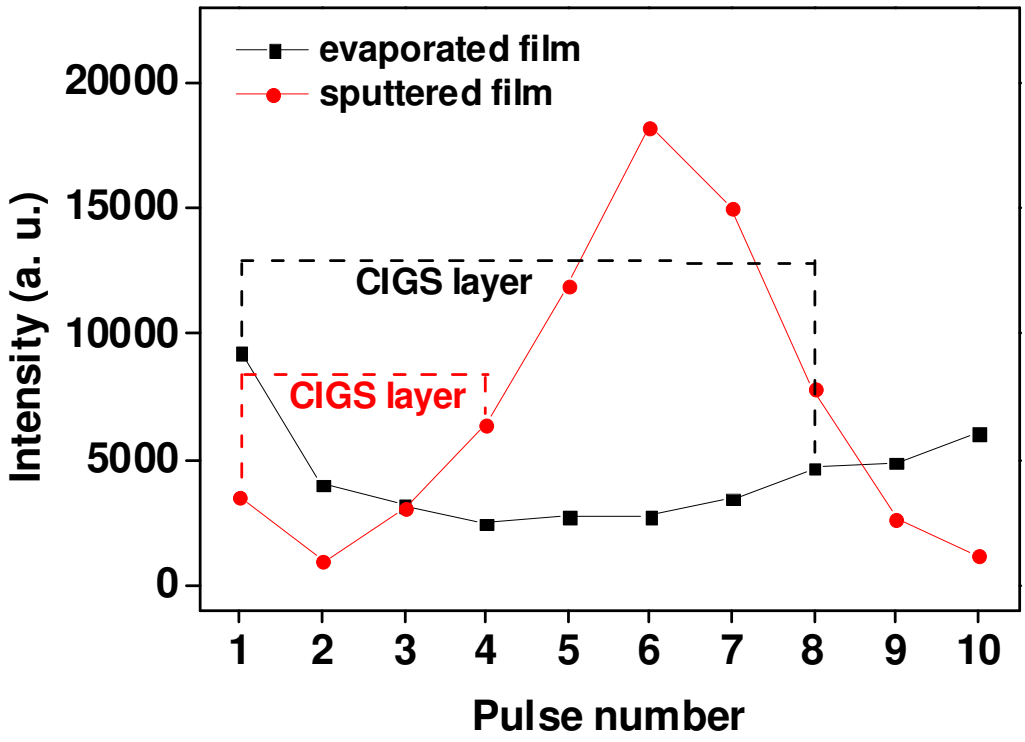

Fig. 10. Intensity variation of the Na line at 589.593 nm with respect to laser pulse number.